Three-Dimensional Modeling of the Solar Active Region*)

Satoshi INOUE and Yasuhiro MORIKAWA

National Institute of Information and Communications Technology (NICT), Tokyo 184-8795, Japan

(Received 7 December 2010 / Accepted 7 March 2011)

In this study we developed an extrapolation code based on the MHD relaxation method to reconstruct a three-dimensional (3D) coronal magnetic field. A 3D magnetic field based on a nonlinear force-free field (NLFFF) was extrapolated from a photospheric vector-field map. A benchmark test using the semi-analytical solution introduced by Low & Lou (1990) found that the extrapolated solution were able to well reproduce an original Low and Lou solution. We then applied the NLFFF extrapolation to solar active region (AR) NOAA 10930. The energy accumulation region formed by the strong magnetic shear above the polarity inversion line was resultantly reproduced and this structure is greatly different from the potential field characterized by the minimum energy state. In this paper we discuss the reliability of our extrapolated field and a relationship between quasi-separatrix layers (QSLs) and a flare ribbon from the CaII image observed by *Hinode/SOT*.

Keywords: solar corona, solar active region, magnetic field, solar flares

DOI: 10.1585/pfr.6.2401067

1. Introduction

The source of solar coronal dynamics that show strong nonlinearity of plasma dynamics is derived from the release of magnetic energy. Solar flares and coronal mass ejections (CMEs) in particular are dynamic phenomena in our heliosphere, and these phenomena cause electromagnetic disturbance as magnetic substorms and ionospheric storms in our geo-space. Understanding the trigger mechanism and dynamics of solar flares, along with the formation and propagation process of the CMEs, are therefore key processes for space weather forecasts. The energy source of these solar explosions is solar active regions that are composed of large sunspots as the cross-section of the strong magnetic flux and have strong magnetic activity. Therefore, it is first important to understand the 3D magnetic field in the solar active region. Unfortunately, 3D coronal magnetic fields cannot be directly observed by state-of-art solar physics satellites and we can only obtain information on magnetic fields on the photosphere from the observations. Coronal magnetic fields are widely believed to satisfy the force-free condition,

$$\nabla \times \boldsymbol{B} = \alpha \boldsymbol{B}, \tag{1}$$

where $\boldsymbol{B}$ is a magnetic field, and α is generally a function of space, because the magnetic pressure dominant to the gas pressure of the coronal plasma; *i.e*, satisfied low β condition in the solar corona. Therefore, a 3D coronal magnetic field is demanded in order to satisfy the force-free condition based on the vector-field data on the bottom boundary. If parameter α corresponds to zero or a constant value; *i.e.*, a potential field or linear force-free field (LFFF), we can easily obtain a 3D coronal magnetic field. However, parameter α is not a constant value but variable in the space. Therefore, because the equation cannot be analytically solved derived from inherent nonlinearity, we developed a numerical code for a nonlinear force-free field (NLFFF) extrapolated from the photospheric magnetic field as a boundary value problem.

In this paper, we first check the reliability of our NLFFF extrapolation code using the semi-analytical solution introduced by Low & Lou [1]. Next, we apply our extrapolation code to NOAA 10930, causing an X3.4 flare, CMEs and electromagnetic disturbance in our geo-space. Japan's solar physics satellite *Hinode* was able to observe the solar flare in this active region and provides the vector-field map obtained from a solar optical telescope(SOT). We report on the relativity of our NLFFF and discuss the 3D structure of NOAA 10930.

2. Numerical Method

NLFF extrapolation methods have been proposed by many researchers [2], and most concepts are as follows. First the boundary condition is fixed as the vector-field map obtained from the observation, then the equation is solved satisfying the force-free condition and searching for the best-fit solution with the observation. This study employs the MHD equation neglected the gas pressure, and gravity under the low β condition.

$$\frac{\partial \boldsymbol{v}}{\partial t} = -(\boldsymbol{v} \cdot \nabla)\,\boldsymbol{v} + \frac{1}{\rho}\boldsymbol{J} \times \boldsymbol{B} + \nu \nabla^2 \boldsymbol{v}, \tag{2}$$

$$\frac{\partial \boldsymbol{B}}{\partial t} = \nabla \times (\boldsymbol{v} \times \boldsymbol{B} - \eta \boldsymbol{J}) - \nabla \phi, \tag{3}$$

$$\boldsymbol{J} = \nabla \times \boldsymbol{B}, \tag{4}$$

author's e-mail: inosato@nict.go.jp

*) This article is based on the presentation at the 20th International Toki Conference (ITC20).

$$\frac{\partial \phi}{\partial t} + c_h^2 \nabla \cdot \boldsymbol{B}, = -\frac{c_h^2}{c_p^2}\phi, \tag{5}$$

where $\boldsymbol{B}$ is the magnetic flux density, $\boldsymbol{v}$ the velocity, $\boldsymbol{J}$ the electric current density, ρ the pseudo-density, and ϕ the convenient potential, respectively. The pseudo-density is assumed to be proportional to $|\boldsymbol{B}|$ in order to ease the relaxation by equalizing the Alfven speed in space. Equation (5) was originally introduced for the algorithm for MHD calculation in [3] in order to avoid deviation from the solenoidal condition $\nabla \cdot \boldsymbol{B} = 0$. The non-dimensional resistivity η is given by a functional

$$\eta = \eta_0 + \eta_1 \frac{|\boldsymbol{J} \times \boldsymbol{B}||\boldsymbol{v}|^2}{|\boldsymbol{B}|}. \tag{6}$$

The η_0 and η_1 are uniform resistivity given by 5.0×10^{-5} and 1.0×10^{-3}. The second term acts well accelerating the relaxation to the force-free field, particularly in the weak field region. The other parameters c_h and c_p are fixed to constant values. The length, magnetic field, velocity, time, and electric current density are normalized by L_0, B_0, $V_A \equiv B_0/(\mu_0\rho_0)^{1/2}$ $\tau_A \equiv L_0/V_A$ $J_0 = B_0/\mu_0 L_0$. The non-dimensional viscosity ν is set as a constant value. The numerical scheme for this calculation is given by the Runge-Kutta-Gill scheme with the fourth-order accuracy for the temporal integral and a central finite difference with the second-order accuracy for a spatial derivative.

3. 3D Magnetic Structure from NLFFF

3.1 Case1 : Low & Lou

First, we check the accuracy of our developed code using the semi-analytical solution introduced by Low & Lou [1]. This is given as a solution of a Grad-Shafranov equation, which is analytically and numerically solved. Figure 1a shows the Low & Lou solution, where the lines indicate magnetic field lines and the normal component of the magnetic field is plotted in a color map. We reconstruct NLFFF only from boundary conditions obtained from the Low & Lou solution. In this case, all boundary conditions are given by the three components of the magnetic field obtained from the Low & Lou solution, the velocity field set to zero at all the boundaries, and a Neumann-type boundary condition ($\partial_n \phi = 0$) is applied for the potential ϕ at all the boundaries: where ∂_n represents the derivative for normal direction on the surface. Parameters are set at $L_0 = 1.0$, $B_0 = 1.0$, $c_p = 0.1$, $c_h = 0.2$ and $\nu = 1.0 \times 10^{-3}$. The simulation domain is a rectangular box spanning $(0, 0, 0) < (x, y, z) < (2L_0, 2L_0, 2L_0)$ and divided by $64 \times 64 \times 64$ grids. An initial condition is given as a potential field calculated from a normal component of the magnetic field on all boundaries. Figure 1b shows the extrapolated magnetic field from the boundary conditions of the original Low & Lou solution. From these results, the extrapolated field is almost the same profile as Low & Lou solution. We also calculate $E_n = \frac{1}{M}\sum_i \{|\boldsymbol{b_i} - \boldsymbol{B_i}|/|\boldsymbol{B_i}|\}$ introduced by [2] to estimate quantitative comparison, where $\boldsymbol{B}_i$ and $\boldsymbol{b}_i$ indicate original and extrapolated solutions and M is a total grid number. As a result, our extrapolated field reach at $1 - E_n = 0.95$ in the whole numerical box and $1 - E_n = 0.99$ in the half box defined by the solid square in Fig. 1b. This result indicates NLFFF can be well reconstructed and small errors are stored near the lateral and top boundaries. Therefore, if the energy stored region in a solar active region is set on the central part in the numerical box, we can expect good reconstruction for the most important part.

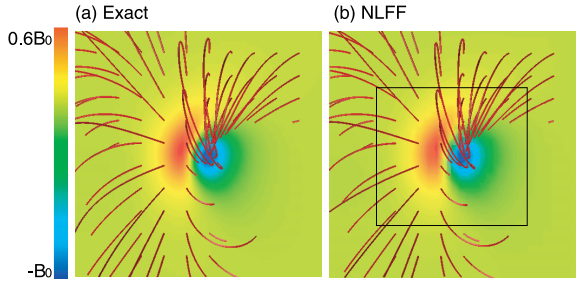

Fig. 1 (a) The left figure shows the exact solution introduced by Low & Lou. The red lines indicate the field lines and the color map shows the normal component of the magnetic field. (b) The right figure shows the NLFFF extrapolated from all boundary conditions.

3.2 Case2 : AR NOAA10930

Next, we reconstruct the AR NOAA 10930 using the vector-field (Fig. 2a) obtained from the *Hinode* satellite by a Milne-Eddington inversion of FeI lines at 630.15 nm and 630.25 nm and the simulated annealing method to solve the 180-degree uncertainty [4]. This is observed at 20:30 UT on December 12th corresponding to the six hours before a flare onset. However, the lateral and top boundaries cannot be provided since these areas are out of the observations. Therefore, these boundary conditions are given by the potential field extrapolated from the line-of-sight of the magnetic field using a synoptic map observed by *The Michelson Doppler Imager on the Solar and Heliospheric Observatory* (*SOHO/MDI*). The critical difference between *Hinode/SP* and *SOHO/MDI* data is that *Hinode* can provide the three components of the magnetic field on the photosphere, whereas the *SOHO/MDI* provides only line-of-sight components. The tangential components on the photosphere are important for reconstructing the energy stored field, therefore *Hinode/SP* data plays an important role for reconstructing a region where a flare occurs. After adjusting the total magnetic flux between the bottom boundary (*Hinode/SOT* + *SOHO/MDI*) and others (*SOHO/MDI*), the potential field given as an initial condition is recalculated from normal component of the magnetic field on all boundaries, and an iteration is performed until the mag-

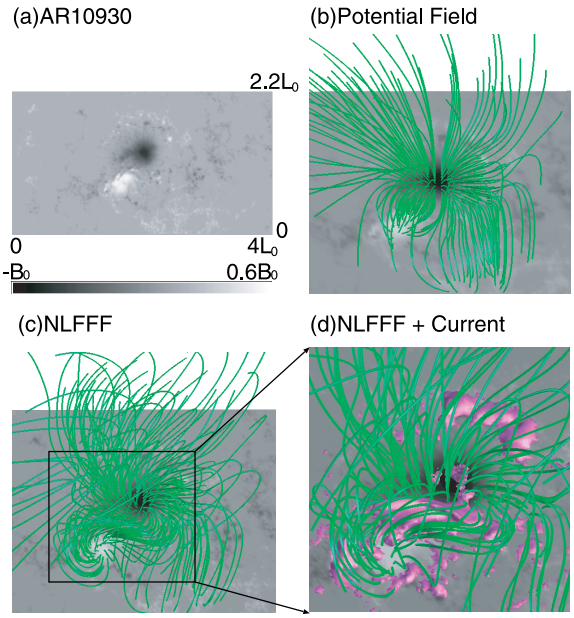

Fig. 2 (a) The normal component of the magnetic field corresponding to the location of the sunspot is plotted in black and white. (b) The 3D potential field is represented on the normal component of the magnetic field. The green lines indicate the magnetic field lines. (c) 3D NLFFF is shown in the same format as (b). (d) The elongated view in a solid square is represented. The purple surfaces indicate a strong current region($|\boldsymbol{J}| = 0.3$).

netic field converge toward to an equilibrium condition. In this case, parameters are set at $L_0 = 5.325 \times 10^9$(cm), $B_0 = 3957$(G), $c_h = 0.2$, $c_p = 0.1$, and $\nu = 1.0 \times 10^{-3}$ and the simulation domain is a rectangular box spanning $(0, 0, 0) < (x, y, z) < (4.0L_0, 2.2L_0, 2.2L_0)$, which corresponds to (295.2″, 162.3″, 162.3″) and uniformly divided by 256 × 128 × 128 grids. The vector-field (250 × 128 grids) from *Hinode* has also been formed by binning from the original vector-field of 1000 × 512 grids. The left area (6 × 128) is covered by *SOHO/MDI* data where three components of the magnetic field are fixed by the initial potential field. The boundary condition is almost same as the Low & Lou case except setting the tangential component of the magnetic field on the top and lateral boundaries. In this case, the tangential component of the magnetic field, except for bottom boundary, is determined by an induction equation (3) during an iteration, while the normal component is fixed with an initial condition to conserve the magnetic flux in the whole domain. This procedure can lead to force-free condition on the top and lateral boundaries due to propagation of the magnetic shear along the magnetic field lines from the bottom boundary.

Figures 2b and c show the potential field given as an initial condition, and NLFFF obtained from a boundary value problem. The lines indicate the magnetic field lines and the color map plotted in black and white shows the normal component of the magnetic field. We found that the region surrounded by the solid square, above the polarity inversion line, is much different from the potential field. Figure 2d is an enlarged view of Fig. 2c and the purple isosurface indicates the strong current region where the magnetic energy in this active region is stored. These results are consistent with [5], and [6].

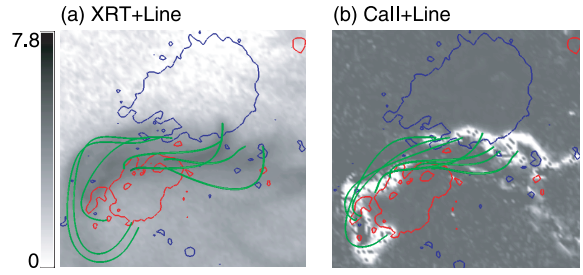

Fig. 3 (a) Selected field lines are plotted over the X-ray intensity map obtained from *Hinode/XRT*. The blue and red contours indicate the location of the negative and positive polarities. (b) Other selected field lines are plotted over the CaII image obtained from *Hinode/SOT*.

We compared the extrapolated field lines with observational data from *Hinode/XRT* to evaluate its reliability. Strong X-ray intensity is widely believed to correspond to the location of the magnetic shear, but the 3D structure of that is not clarified by the 2D image provided by observations. Figure 3a shows the selected field lines plotted on the X-ray intensity map observed by *Hinode/XRT* at 20:30 UT on December 12th. We found that these sheared field lines correspond to the strong X-ray intensity region which is composed of differently shaped field lines. This result is consistent with [7,8], and [9] in the previous study. We also compared the extrapolated field lines with observational data from *Hinode/SOT*. Since flare ribbons are widely believed to illuminate simultaneously on the regions corresponding to the feet of the reconnected magnetic field lines ([10–13]), we can evaluate how well the model field may capture the coronal magnetic field by inspecting the agreement between the ribbons and the feet of the field lines. This analysis also helps our understanding of the field lines structure in the flaring site. Figure 3b represents a flare ribbon at 02:22 UT on December 13th in the color map and selected field lines traced from the ribbon on the negative pole. From this result, it is found that the location of the footpoints of magnetic field lines corresponds well to the flare ribbon. These results indicate the NLFFF effectively reproduces the complicated 3D structure of the magnetic field in the flaring region, even though the artificial boundary conditions are imposed on the lateral and top boundaries and furthermore the vector-field data is observed six hours before observation of Ca II.

Finally, we investigated the relationship between magnetic topology of field lines and the flare ribbon from the CaII image obtained from *Hinode*. The magnetic topology is defined as the photospheric cross-section of the quasi-separatrix layers (QSLs) introduced by [14]. We calcu-

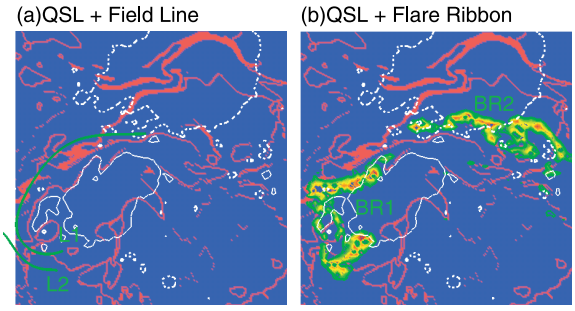

Fig. 4 (a) The red lines indicate the distribution of $N(x, y) > 25$ defined in equation (7). The green lines indicate the field lines. The solid and dotted white lines represent the positive (790 G) and negative (−790 G) polarities of the normal component of the magnetic field. (b) An image of the flare ribbons observed at 02:22 UT on December 13th is plotted over (a).

lated the following quantity at each pixel on the vector-field maps:

$$N(x, y) = \sqrt{\sum_{i=1,2}\left[\left(\frac{\partial X_i}{\partial x}\right)^2 + \left(\frac{\partial X_i}{\partial y}\right)^2\right]}, \quad (7)$$

where (X_1, X_2) is the relative distance corresponding to the $(x' - x'',\ y' - y'')$. (x', y') and $(x'',\ y'')$ are the positions of two end points of a field line on the photospheric surface. Figure 4a represents distribution $N(x, y)$ mapped on the photosphere. The solid and dotted white lines indicate the positive and negative normal components of the magnetic field. The magnetic field lines are represented by the green lines named by L1 and L2. In this figure, $N(x, y) > 25$ is in red and we clearly find that the red is not widely distributed but in a thin layered structure. We also find that field lines change drastically across these red layers such as L1 and L2. Figure 4b shows the flare ribbons BR1 and BR2 observed by *Hinode/SOT* at 02:22 on December 13th over the $N(x, y)$ distribution. These results indicate that BR1 seems to be along with the part of the layer of $N(x, y)$. Because the flare ribbon is widely believed to correspond to the footpoint of reconnected field lines, this well corresponds to the footpoint of separatrix. On the other hand , the BR2 profile is slightly deviates from the layer of $N(x, y)$. Though this reason is not yet clarified, one reason for this deviation may be derived from the time gap between two different observations.

4. Summary

Our results show a flare producing magnetic structure is already formed six hours before a flare onset and the location of the flare ribbon may have a relation with the $N(x, y)$ layers. If we were able to obtain the vector-field map six hours before a flare onset, we may be able to reconstruct the flare-producing magnetic field and suggest the flare ribbon profile from the $N(x, y)$ distribution. However, these results are just one of examples and all results do not necessarily correspond to the ours. Therefore, we will have to perform the statistical analysis using other solar active regions. Unfortunately, though NLFFF can tell us the quasi equilibrium condition before a flare, the flare dynamics cannot be clarified from it. In previous numerical studies for flare dynamics, ideal initial conditions far from real magnetic configuration in the solar corona have been assumed such as [15], or [16], and summarized in [17]. However, we expect the further understanding by applying NLFFF to numerical studies and we may advance towards the realization of space weather.

The one of author (S.I) thanks to profs. K. Kusano, T. Magara, Drs. D. Shiota and T.T. Yamamoto for useful discussions. This work was supported by a Grant-in-Aid for an incentive study of the NICT President's Fund. The ambiguity resolution code used herein was developed by K. D. Leka, G. Barnes, A. Crouch with NWRA support from SAO under NASA NNM07AB07C.Hinode is a Japanese mission developed and launched by ISAS/JAXA, with NAOJ as domestic partner and NASA and STFC (UK) as international partners. It is operated by these agencies in co-operation with ESA and NSC (Norway). The supercomputer system, data analysis and visualization system of this work were done by using resources of the Cybermedia Center of Osaka University and the OneSpaceNet in the NICT Science Cloud.

[1] B.C. Low and Y.Q. Lou, ApJ **352**, 343 (1990).
[2] C.J. Schrijver *et al.*, Solar Phys. **235**, 161 (2006).
[3] A. Dedner, F. Kemm, D. Kröner, C.-D. Munz, T. Schnitzer and M. Wesenberg, J. Comput. Phys. **175**, 645 (2002).
[4] K.D. Leka, G. Barnes and A. Crouch, ASP Conf. Series **415**, 365 (2009).
[5] C.J. Schrijver *et al.*, ApJ **675**, 1637 (2008).
[6] S. Inoue *et al.*, ASP Conf. Series **397**, 110 (2008).
[7] T. Magara and D.W. Longcope, ApJ **559**, L55 (2001).
[8] D.E. McKenzie and R.C. Canfield, A&A **481**, L65 (2008).
[9] V. Archontis, A.W. Hood, A. Savcheva, L. Golub and E. Deluca, ApJ **691**, 1276 (2009).
[10] H. Carmichael, NASA Special Publication **50**, 451 (1964).
[11] P.A. Sturrock, Nature **211**, 695 (1966).
[12] T. Hirayama, Solar Phys. **34**, 323 (1974).
[13] R.A. Kopp and G.W. Pneuman, Solar Phys. **50**, 85 (1976).
[14] P. Demoulin, J.C. Henoux, E.R. Priest and C.H. Mandrini, A&A **308**, 643 (1996).
[15] K. Kusano, T. Maeshiro, T. Yokoyama and T. Sakurai, ApJ **610**, 537 (2004).
[16] S. Inoue and K. Kusano, ApJ **645**, 742 (2006).
[17] M.G. Linton and M.B. Moldwin, J. Geophys. Res. (Space Physics) **114**, A00B09, doi:1029/2008JA013660, 2009 (2009).